Circular polarized light microscopy to investigate the crystal orientation of aluminium.

[a,b]Hamed Safaie, [a,b]Mark Coleman, [a,b]Richard Johnston, [a]Amit Das, [a,b]James Russell,
[a,b]Cameron Pleydell-Pearce

[a]Swansea University, Faculty of Science and Engineering, Fabian Way, Crymlyn Burrows,
Swansea, Wales, UK SA1 8EN.

[b]Swansea University, Advanced Imaging of Materials (AIM), Faculty of Science and
Engineering, Fabian Way, Crymlyn Burrows, Skewen, Swansea, Wales, UK SA1 8EN.

Abstract

The link between microstructure, crystallographic texture and mechanical properties is of substantial importance to the understanding of materials behaviour of aluminium alloys. The favoured approach to determine these relations has been electron backscatter diffraction (EBSD) and has received extensive prior attention. However, compared to conventional optical microscopy, EBSD is both cost and potentially time intensive limiting its viability as a widespread method in industrial quality assurance. Following early successes by the authors and other investigators with optically birefringent metals, this investigation assesses the suitability of reflected circular polarized light microscopy (CPLM) as a rapid low-cost alternative to EBSD for cubic systems. Direct comparisons between EBSD crystal orientation maps (COMs) and a quantitative determination of the character of reflected polarized light images is presented to demonstrate that this technique can provide quantitative texture information for aluminium. Further, the inherently surface sensitive nature of the technique allowed further verification of orientation relationships between the substrate and surface oxide only previously made possible by high resolution transmission electron microscopy.

Keywords: Crystallography, Electron Backscattered Diffraction, Polarized Light Microscopy, Crystal Orientation Map, Anodized Aluminium.

1. Introduction

The influence of texture (grain orientation distribution) on the mechanical performance of aluminium is well documented [1–3], assisted primarily by crystal orientation mapping (COM) and electron backscatter diffraction (EBSD) [4,5]. Although now widely used, EBSD is still a specialized technique that is both expensive and potentially time consuming for assessing texture characteristics as routine design / quality control criteria in an industrial environment [2,6].

Polarized light microscopy (PLM) is a long-established technique [7], traditionally associated with qualitative phase identification (phase contrast) in a variety of metals and minerals and offers a potential alternative for texture evaluation. A technique primarily applied in transmission; it is by nature restricted to inherently optically anisotropic (birefringent) material. Previous investigations in bioscience applications demonstrated success in resolving differences in optical birefringence behaviour in transmitted light microscopy [8–11]. More recently, it has been applied in reflection for birefringent crystals to investigate microtexture [12,13]. In both cases, determinations of the correlation between birefringence and crystal orientation were made using the linearly cross polarized condition. This has two practical disadvantages; 1) careful simultaneous control of two independent polarizers is required for a stationary sample, or else 2) the sample must be euccentrically rotated 360° and subsequent acquisition data transposed to determine the orientation. Whilst adequate to determine orientation relations, these steps significantly slow the acquisition rate and introduce additional measurement error.

The goal of the present study was to demonstrate two key novel steps in the development of this technique 1) that these practical and optically inherent limitations could be overcome 2) that this new method could be applied to inherently optically isotropic materials. A novel approach to optically determine the microtexture of optically isotropic and cubic material using Circular Polarized Light Microscopy (CPLM) is therefore investigated. This method negates the requirement for complex manipulation of either sample or microscope and is validated by EBSD data acquired through correlative light and electron microscopy (CLEM). The potential flexibility, reliability and speed of this new technique is compared to EBSD with a view to providing recommendations for its wider implementation [4,14–16].

The alloy studied is a model Al-Cu alloy relevant to commercially available 2XXX series aluminium alloys. It is well-established that this alloy group can be anodized to generate qualitative optical orientation contrast [17]. Franklin and Stirland discovered in 1963 that this optical anisotropy is due to variations in pore inclination as the formed Alumina on the surface is in different crystals[18]. This has been previously used to help determine phase proportions and microtextural morphology [14]. However, to the authors knowledge, this has never been used to quantitatively determine the orientation of the underlying crystal, which is attempted here. Further previous research in the field of electrochemistry has examined the development of an oxide layer in the context of surface passivation [18]. These studies determined an orientation relationship between the substrate and nanometre scale oxide through high resolution TEM. This found that the [0001] direction in the HCP oxide was parallel to the [001] direction in the FCC substrate, albeit this was defined from a limited number of cases given the significant complexity in making these measurements. The inherently surface sensitive nature of the proposed technique coupled with the EBSD measurements permits more extensive insight into these observations and the potential for similar approaches with other cubic systems [5,14,15,19] with the potential for impact on the understanding their electrochemical behaviour.

2. EXPERIMENTAL PROCEDURE

2.1 Material Preparation

The model Aluminium-2wt.% Copper alloy used has a low density and good mechanical properties such as a high strength to weight ratio and excellent corrosion resistance [20,21]. The sample was subjected to standard metallographic preparation routes, with a final polish using a Struers OP-S solution with 10% H_2O_2¬ by volume on a Struers MD-Chem medium for 10 minutes. The material was anodized using Barker's reagent (5ml 48%HBF_4 and 200ml H_2O) at a current density $J = 0.2\ A/cm^2$ for 60s at room temperature using a Kristall 680 fully automatic electrolytic polisher and etcher. These conditions were selected to produce the required thickness of alumina on the surface that has been previously determined in the literature [5,22–24].

2.2 EBSD analysis

EBSD data was collected in a Carl Zeiss Crossbeam 550 operated at 20kV and Oxford Instruments Nordlys 2 high speed Camera with Aztec with a step size of 5 microns. The EBSD system was calibrated using a cleaved silicon specimen of known crystallographic orientation to provide a misorientation resolution of 0.5º. The data was acquired before anodizing the sample as the alumina on the sample surface prevented generation of the signal for Kikuchi bands. EBSD data is presented in the form of Crystal Orientation Maps (COMs) employing modified Euler colour distribution (Bunge convention), which is explained in detail later [4,15,46].

2.3 Light path design

All optical microscopy was carried out in a Zeiss Axio Observer inverted microscope though the light source and the light path have been modified specifically for the technique described below. In order to create accurately circular polarized light without a phase shift, monochromatic light of wavelength λ = 440nm was used. This was selected because 1) it permitted a quarter wave plate thickness compatible with the microscope and 2) this wavelength provided the lowest chromatic shift as measured by optical spectrometer through 360º analyzer rotation for the light path under pan-chromatic (LED) illumination. The monochromatic light passed through a linear polarizer at an inclination of 45° to the image vertical direction, then passed through a compatible quarter wave plate with a fast axis of 0° to have an output of circular polarized light [25–27].

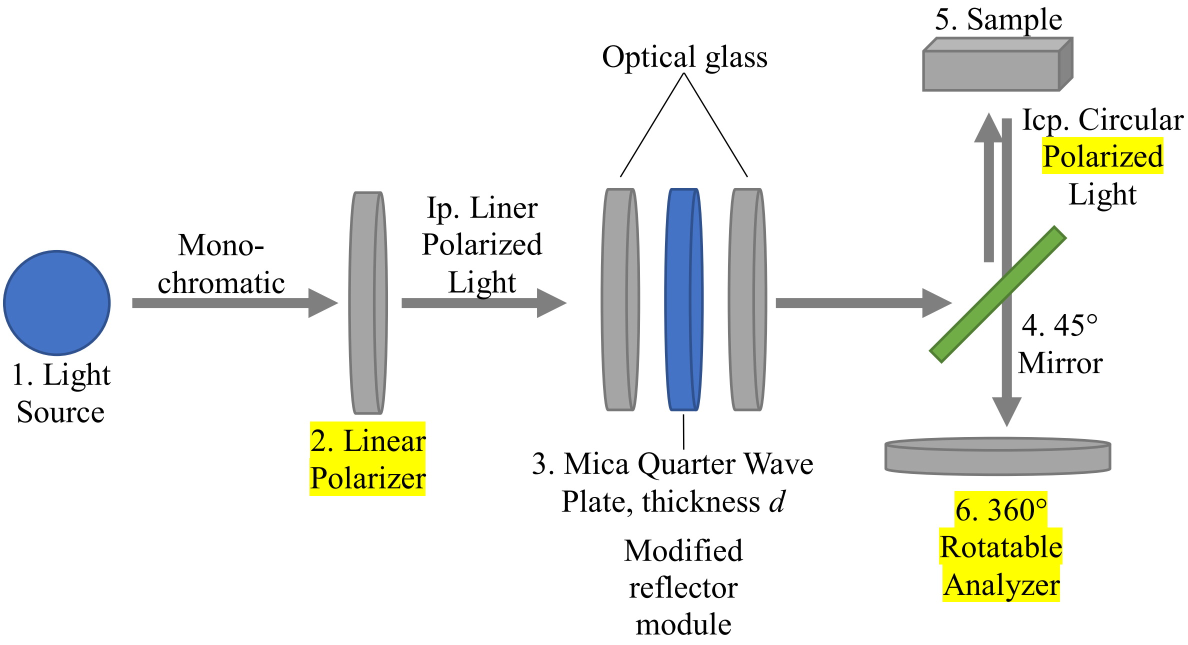

Fig. 1. Optical path for CPLM where 1 is monochromatic light source, 2 is the linear polarizer, 3 is quarter wave plate, 4 is a mirror with angle of 45°, 5 is the sample and 6 is 360° rotatable analyzer.

Mica is a zero order wave plate which means it can be used for a wider range of wavelengths. However, to minimise error, the plate thickness for this particular wavelength needs careful calculation [26,29,30,48] using *Eq 1*.

$$N\lambda = \pm(n_e - n_o)d \rightarrow d = \left|\frac{\lambda}{4(n_e - n_o)}\right|$$

Eq. 1

Where λ is the wavelength of the source light and d is the thickness of the quarter wave plate. N is the retardation which can be expressed as fraction of wavelength, such as quarter wave plate retardation is $N = 1/4$ [28,29]. n_o represents the ordinary and n_e illustrates the extraordinary refractive indices [29].

The fidelity of circular polarization was experimentally verified by capturing the intensity of a mirror reflection through a 360° rotation of the analyzer with the Left Circular Polarized (LCP) light reflected from the mirror to produce a Right Circular Polarized (RCP) state. In this condition the intensity remained consistent independent of the rotation of the analyzer (Fig. 2) demonstrating there is no elliptical character to the light, Fig. 2 proves the ¼ wave plate thickness and wavelength are suitable.

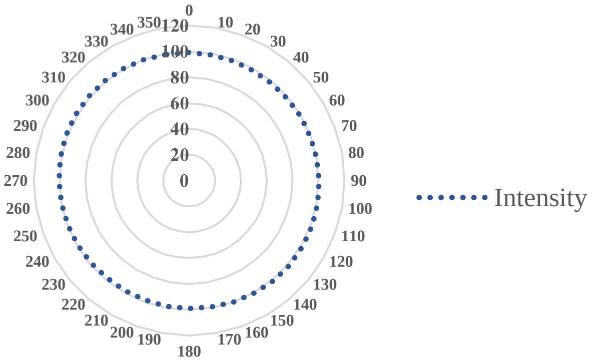

Fig. 2. Intensity plot captured from the mirror reflection of modified circularly polarized light microscopy through 360 degrees of analyzer rotations.

To ensure that the interaction between light and the sample are understood theoretically the following approach was adopted to describe the light path and beam polarization state. The output light polarization state before reaching the sample can be calculated by:

$$S' = (S)\,(Mp)\,(Mr)\,(Mm)$$

Eq. 2

Where S is the stoke parameters of input unpolarized light, Mp is the Mueller matrix for linearly polarizer filter, Mr is the Mueller matrix for a rotator and Mm symbolized the Muller matrix for the mirror. Muller matrices can be used to specify the state of polarizer and the quarter wave plate whilst the character of the beam was described by four different observables stoke parameters (S_0, S_1, S_2, S_3), The first Stokes parameter S_0 describes the total intensity of the light; the second parameter S_1 describes the amount of linear horizontal or vertical polarization, the third parameter S_2 describes the amount of linear +45° or -45° and, finally, S_3 describes the preponderance of right circular polarized light over left circular polarized light. which are represented by Eq. 3.

$$S = \begin{pmatrix} S_0 \\ S_1 \\ S_2 \\ S_3 \end{pmatrix}$$

Eq. 3

The state of unpolarized light, i.e. the monochromatic light source is:

$$S = \begin{pmatrix} S_0 \\ S_1 \\ S_2 \\ S_3 \end{pmatrix} = \begin{pmatrix} 1 \\ 0 \\ 0 \\ 0 \end{pmatrix}$$

The Mueller matrix for a perfect linear polarizer (*Mp*) with transmitted axis at an angle Θ = 45° is:

$$Mp = \begin{pmatrix} 1 & cos2\theta & sin2\theta & 0 \\ cos2\theta & cos^2\theta & sin2\theta cos2\theta & 0 \\ sin2\theta & sin2\theta cos2\theta & sin^2\theta & 0 \\ 0 & 0 & 0 & 0 \end{pmatrix} = \begin{pmatrix} 1 & 0 & 1 & 0 \\ 0 & 0 & 0 & 0 \\ 1 & 0 & 1 & 0 \\ 0 & 0 & 0 & 0 \end{pmatrix}$$

Eq. 4

The Mueller matrix of the quarter plate (*Mr*) with the fast axis of 0° and the phase delay Ø of 90° can be expressed by Eq. 5.

$$Mr = \begin{pmatrix} 1 & 0 & 0 & 0 \\ 0 & 1 & 0 & 0 \\ 0 & 0 & COSØ & -SINØ \\ 0 & 0 & SINØ & COSØ \end{pmatrix} = \begin{pmatrix} 1 & 0 & 0 & 0 \\ 0 & 1 & 0 & 0 \\ 0 & 0 & 0 & -1 \\ 0 & 0 & 1 & 0 \end{pmatrix}$$

Eq. 5

The mirror symmetry relation (*Mm*) represents the Mueller matrix in the following form.

$$Mm = \begin{pmatrix} a & b & 0 & 0 \\ b & a & 0 & 0 \\ 0 & 0 & a & b \\ 0 & 0 & -b & a \end{pmatrix} = \begin{pmatrix} 1 & 0 & 0 & 0 \\ 0 & 1 & 0 & 0 \\ 0 & 0 & -1 & 0 \\ 0 & 0 & 0 & -1 \end{pmatrix}$$

Eq. 6

The state of the output light for this case will then appear as a left circular polarized light (LCPL).

$$S' = \begin{pmatrix} 1 \\ 0 \\ 0 \\ -1 \end{pmatrix}$$

As such the experimental and theoretical approaches agree and demonstrate that the modified incident light path is suitable for the CPLM technique. Therefore any changes in polarization state of light after interaction with the sample can be related to the orientation of the c-axis of optically anisotropic alumina crystals at the surface of an anodized sample that is reasonably free from surface defects [30–33]. This incident condition was fixed for the apparatus and is henceforth referred to as “the incident light”.

3. Result and discussion

3.1 Qualitative analysis

After collecting the EBSD data, the same area was anodized and tested under circular polarized light microscopy. The intensity plot was captured by taking the intensity of each pixel position for images collected at all analyser rotations. Fig. 3A - C represents how each grain appears for different illumination conditions. For pan-chromatic illumination, intensity data acquired under circular polarized light will be recorded by the detector in three different channels of colour (Red, Green and Blue). However, because a monochromatic blue (λ=440), light source was used in this study, the intensity is unaffected by chromatic shift (Fig. 3C).

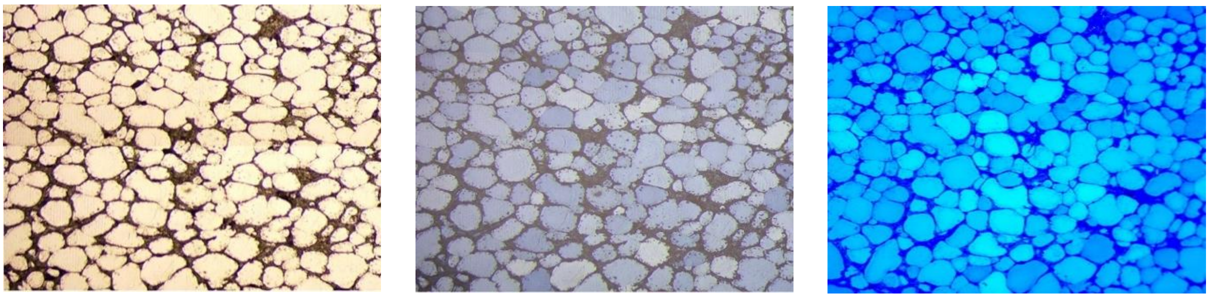

A) Bright filed B) CPLM method with white LED C) Modified CPLM method

Fig. 3. The same area of interest under four different conditions A) Bright field with a LED light B) Circular polarized light microscopy with a LED light C) Circular polarized light microscopy with a monochromatic light.

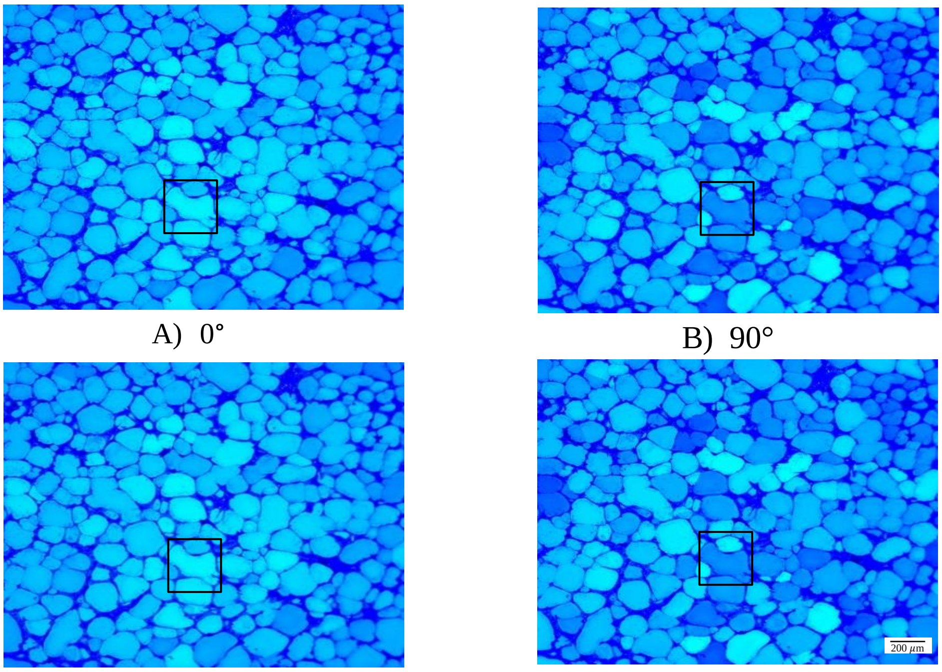

A) 0° B) 90° C) 180° D) 270°

Fig. 4. Qualitative observations of symmetry in the contrast of images recorded under circular polarized light microscopy.

Circular Polarized light images were recorded using rotating analyzer at various sample crystal orientations applied using the highlighted microstructure presented in Fig. 4 as an arbitrary example. Fig. 4 shows the symmetry observed in the appearance of images recorded at 0˚,90˚,180˚ and 270˚ of rotation respectively. Microstructural features appear similar at 0° / 180° and 90°/270° illustrating a 180° symmetry in the retardation behaviour. This observation correlates well with the crystallographic symmetry of both the [0001] direction of the HCP surface oxide and the [001] direction of the (FCC) substrate system [49,50] which can be linked according to the previously reported orientation relationship [18]. Moreover, as the analyzer was rotated, the intensity associated with individual units was found to vary sinusoidally against rotation with a phase of approximately 180° as demonstrated in Fig. 5. This represents the intensity value for an individual grain from the dataset in Fig. 5 with a crystal orientation of φ1 = 157˚, Φ = 42˚ and φ2 = 22˚. The effect of symmetry appears clearly in the plot as the FCC crystal orientation symmetry for φ1=180°. The unit cell symmetry suggests that data captured from only 0° to 180° or 180° to 360° is needed to correlate the CPLM data to EBSD.

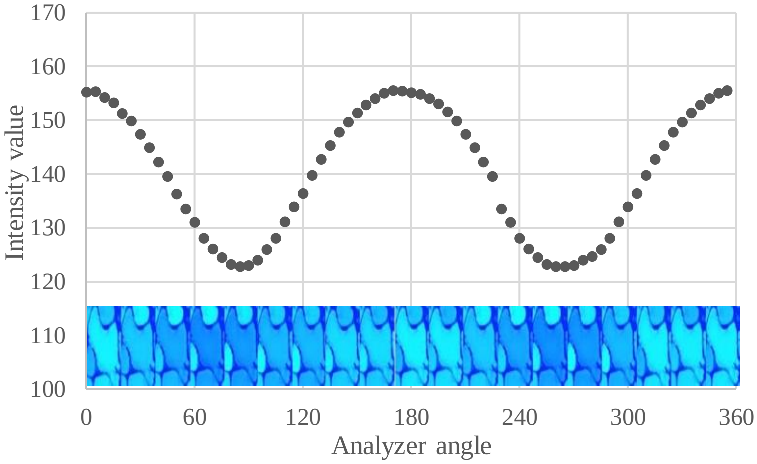

Fig. 5. An intensity profile and its derivative for an individual crystal orientation recorded over a complete analyzer rotation.

3.2 Quantitative analysis

Fig. 6 plots the intensity profiles of two grains with similar crystal orientations. Both grains give intensity maxima and minima at similar analyzer rotation angles and both show comparable differences in maximum and minimum intensity, i.e. profiles are similar and the intensity difference (ΔI) remains constant, even though the absolute intensity values are different.

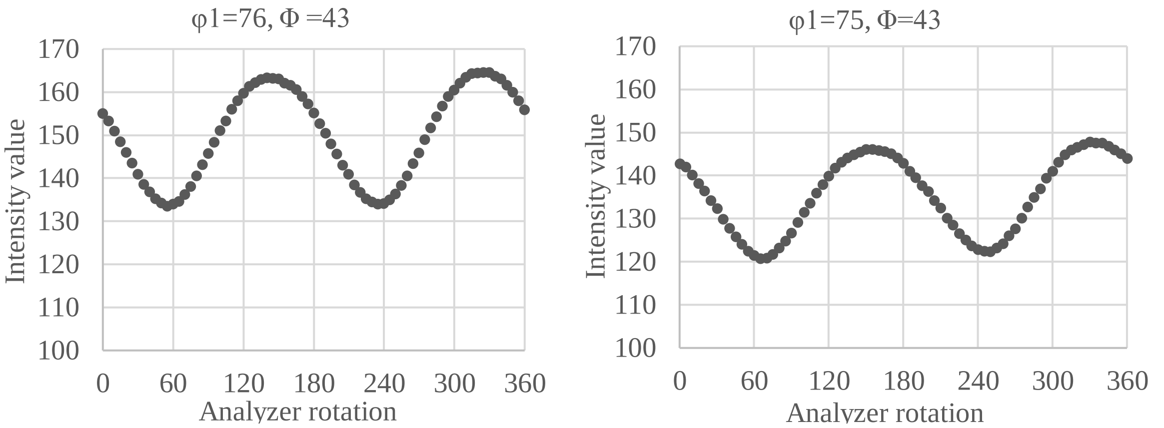

Fig. 6. CPLM intensity data of Close C axis crystals orientations. Left intensity plot is φ1=76 and Φ=43, Right intensity plot is φ1=75, Φ=43

This proves that areas of common orientation can be measured by employing CPLM technique. To explore this for a wide range of orientations, the reference coordinate data for φ1 collected from EBSD was compared directly with the CPLM intensity data. Fig. 7A presents the correlation between Euler 1 (φ1) and the maximum intensity observed through 180 degrees rotation of the analyzer from 180° to 360°. This data represents the position of maximum intensity shifting from 360° to 180° as the Euler 1 (φ1) is increased from 0° to 180°. Fig. 7B presents the correlation between the difference in maximum and minimum intensity (ΔI) to Euler 2 (Φ). The symmetry of Φ is distinguished to be 45° for FCC according to Gert Nolze 2015 [50]. The plot illustrates that by increasing Φ, ΔI for a specific grain would appear more noticeable. It follows that these two parameters are the main reference points required to create the c-axis map for the surface oxide and by inference the [001] FCC direction.

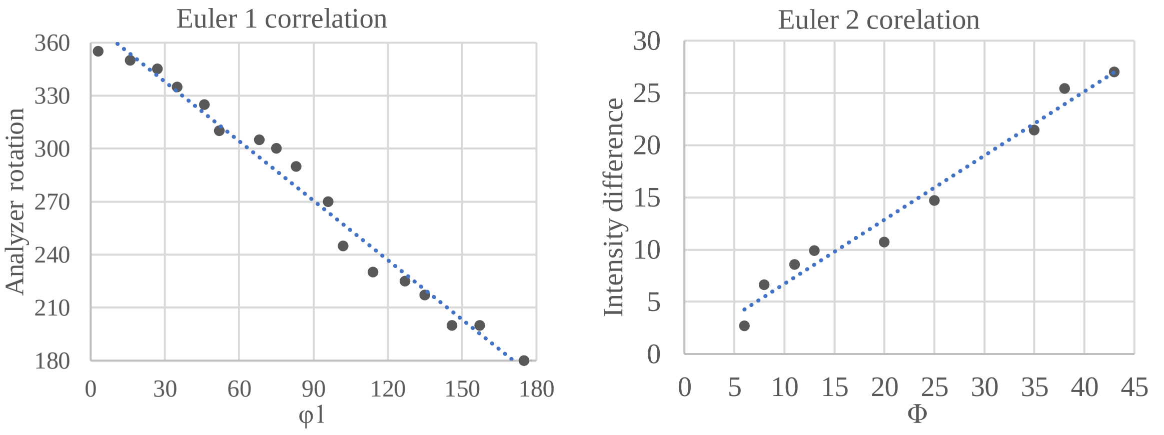

A) B)

Fig.7. Correlation plots of CPLM data and EBSD data. A) Euler 1 correlation Plot represents the correlation between Euler 1 (φ1) and analyzer rotation. B) Euler 2 correlation illustrates the connection between the difference of maximum and minimum intensity to the Euler 2 (φ).

3.3 Theoretical validation of the observed incident beam rotation after reflection

We have shown that there is a correlation between φ1 and the analyser position that yields the maximum intensity over 180° of rotation (Fig. 7A). From a theoretical perspective this is equivalent to Θ in Eq. 4 and that equation can be used to calculate the linear parameter of polarized light reflected from the sample. This parameter is described by the S_1 and S_2

components of the Stokes vector. These values for equivalent analyzer rotations to those in the experimental data (Fig 7A) are presented in table 1.

Table 1. The stoke parameter value for S_1 and S_2 over the rotation of 180° of analyzer rotation.

Analyzer rotation	0°	15°	30°	45°	60°	75°	90°	105°	120°	135°	150°	165°	180°
S_1	1	0.866	0.5	0	-0.5	-0.866	-1	-0.866	-0.5	0	0.5	0.866	1
S_2	0	0.5	0.866	1	0.866	0.5	0	-0.5	-0.866	-1	-0.866	-0.5	0

We have also shown that ΔI reaches a maximum as Φ reaches 45° (Fig. 7B). This intensity change during the reflection of circularly polarized light has been previously shown to be related to the ellipticity parameter of the Stokes vector and describes the change from circular to linear polarization (Fig. 8) [7,30,32–34]. To mathematically validate our observations against this theory, the following approach is adopted:

The transverse components of light are represented by Eq.7.

$$E_x(z,t) = E_{0x}\, cos(\tau + \delta_x)$$

Eq. 7.a.

$$E_y(z,t) = E_{0y}\, cos(\tau + \delta_y)$$

Eq. 7.b.

Where t represents the time, E_{0x} and E_{0y} are the maximum amplitudes of the optical field and τ is the propagator which is constant. The subscripts x and y refer to the component direction in x and y. The propagation of Ex and Ey give rise to a vector describing a locus of points in space that generates a curve whose form can be derived using the equations 7.a and 7.b.

$$\frac{E_x}{E_{0x}} = cos\, \tau\, cos\, \delta_x - sin\, \tau\, sin\, \delta_x$$

Eq. 8.a.

$$\frac{E_y}{E_{0y}} = cos\, \tau\, cos\, \delta_y - sin\, \tau\, sin\, \delta_y$$

Eq. 8.b.

Rearranging the terms of equation 8 and subtracting using the double angle formula gives

$$\frac{E_x}{E_{0x}} sin\delta_y - \frac{E_y}{E_{0y}} sin\delta_x = \cos\tau \sin(\delta_y - \delta_x)$$

Eq. 9.a.

$$\frac{E_x}{E_{0x}} \cos\delta_y - \frac{E_y}{E_{0y}} \cos\delta_x = \sin\tau \sin\left(\delta_y - \delta_x\right)$$

Eq. 9.b.

Squaring equation 9 and adding them together gives the equation for parameters of the polarization ellipse:

$$\frac{E_x^2}{E_{0x}^2}+\frac{E_y^2}{E_{0y}^2}-\frac{2E_xE_y\cos\delta}{E_{0x}E_{0y}}=\ sin^2\delta$$

Eq. 10.

Where δ = δx – δy (the phase difference).

This signifies that if the incident light is reflected back from a crystal with Φ= 0° it will be reflected in the RCP state.

In this condition (δ = Л/2 and E_{0x} = E_{0y} = E_o)

$$\frac{E_x^2}{E_{0x}^2}+\frac{E_y^2}{E_{0y}^2}-\frac{2E_xE_y\cos\delta}{E_{0x}E_{0y}}=\ sin^2\delta \text{ leads to } \frac{E_x^2}{E_{0x}^2}+\frac{E_y^2}{E_{0y}^2}\ =1$$

According to cubic crystal symmetry the maximum value for Φ without describing an indistinguishable reflection is 45°. In this condition (δ=0 and E_ox = E_oy) giving:

$$\frac{E_x^2}{E_{0x}^2}+\frac{E_y^2}{E_{0y}^2}-\frac{2E_xE_y\cos\delta}{E_{0x}E_{0y}}=\ sin^2\delta \text{ leads to } \left(\frac{E_x}{E_{0x}}+\frac{E_y}{E_{0y}}\right)^2\ =\ 0$$

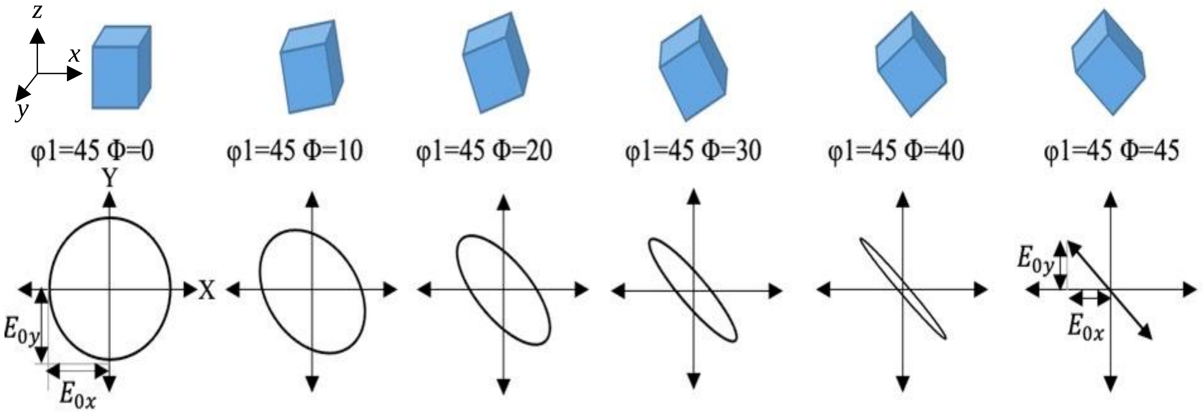

Fig. 8. The effect of Φ rotation on the ellipse amplitude.

When this theoretical calculation of the Ellipticity parameter (Fig. 9A) under perfect conditions was compared with the experimentally observed intensity data, (Fig. 9B) it followed and inverse relationship. This confirms that the Ellipticity parameter (or the value of S_3) which can be determined by ΔI is dependent on the Φ component of the crystal orientation.

By combining the observations presented in Figs (7A) and (7B) with the theoretical descriptions presented above it is possible to unambiguously determine the polarization state. This can be represented on the Poincare sphere (Fig. 11), which is a common way to illustrate the state of the light reflected from the sample [35] but is less useful for quantitative observations. Instead here we have for the first time unified theoretical and experimental descriptions of the polarization state with the crystal orientation. The relationship between the intensity profile and the polarization state is illustrated in Fig. 10, where Ψ is the analyzer position of maximum intensity and X is ΔI. With reference to the theoretical description outlined above, the Stoke parameters can then be expressed in terms of Ψ and X. The approach taken to calculate the Stoke parameters and relate them to experimentally determined crystal orientation is shown in equations 11-13 below [7,34–40, 47]. For convenience, various examples comparing the measured and calculated outcomes are presented in table 2.

$$S_1 = cos(2X)cos(2\Psi)$$

Eq. 11

$$S_2 = cos(2X)\sin(2\Psi)$$

Eq. 12

$$S_3 = \sin(2X)$$

Eq. 13

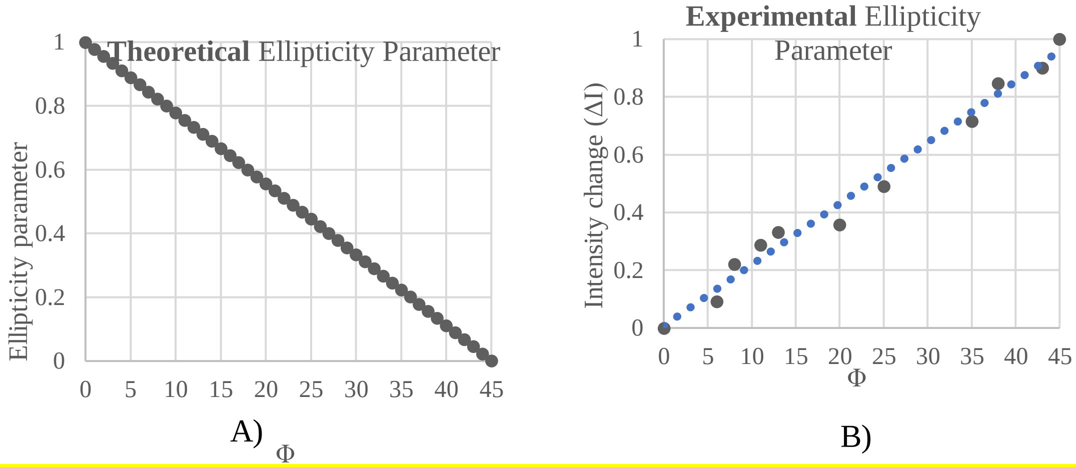

A) B)

Fig. 9. Correlation between ellipticity parameter and the difference between max and min intensity (ΔI value) for a) theoretically calculated ellipticity parameter and b) experimentally measured ellipticity parameter.

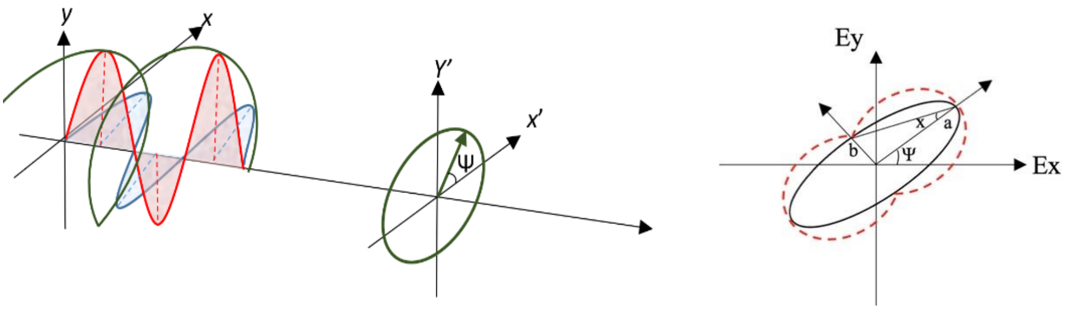

A) B)

Fig. 10. A) Formation of an elliptical ellipse by electrical field at the coordination of Ψ. B) Elliptical polarized ellipse corresponding to the intensity profile. Ψ is the orientation angle of the ellipse and X the measure of the ellipticity. a is the major axis and b is the minor axis.

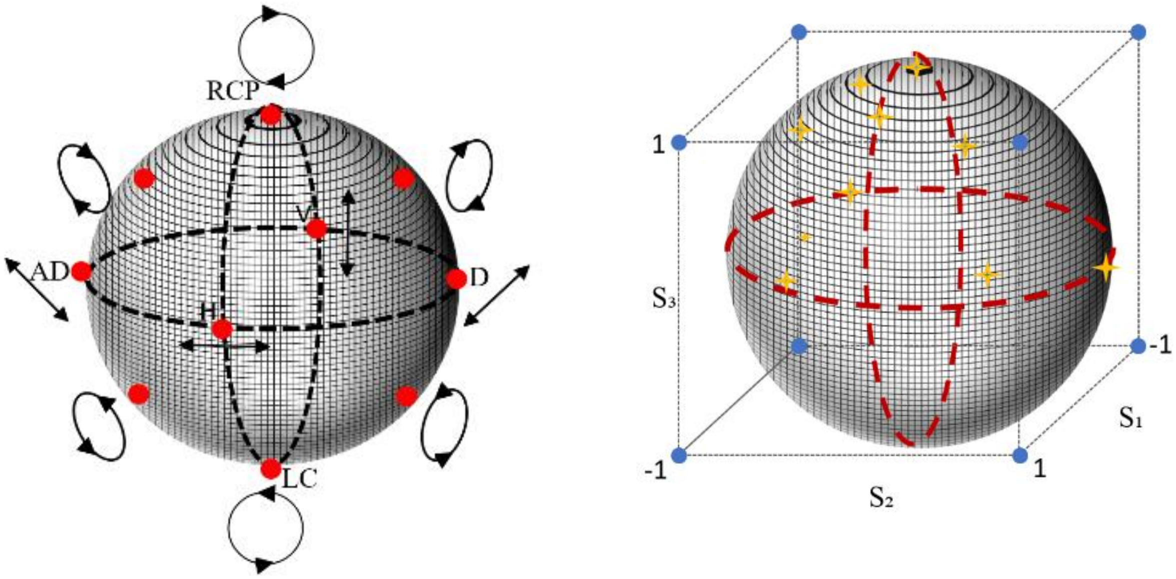

Fig 11. Representation of polarization state of table 3 on a Poincare sphere. A) General format of Poincare sphere representing systematic range of polarization state. B) Representation of polarized ellipse in table 3 on Poincare sphere

Table 2. Ellipse structure and stoke parameters for different range of crystal orientation.

C axis Euler angle (EBSD)	φ1=14° Φ=0°	φ1=111° Φ=6°	φ1=33° Φ=8°	φ1=201° Φ=11°	φ1=271° Φ=13°
Shape of the ellipse (CPLM)	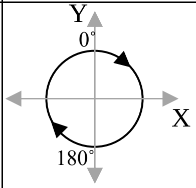	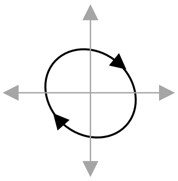	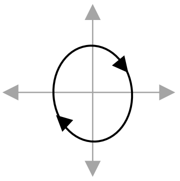	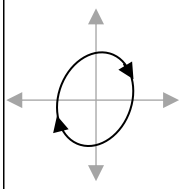	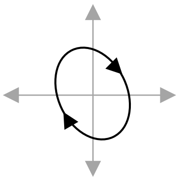
Maximum intensity angle(CPLM)	NA	130°	175°	20°	155°
Stoke parameters	$S_{out}=\begin{pmatrix}1\\0\\0\\1\end{pmatrix}$	$S_{out}=\begin{pmatrix}1\\-0.035\\-0.203\\0.978\end{pmatrix}$	$S_{out}=\begin{pmatrix}1\\0.27\\-0.04\\0.96\end{pmatrix}$	$S_{out}=\begin{pmatrix}1\\0.28\\0.23\\0.92\end{pmatrix}$	$S_{out}=\begin{pmatrix}1\\0.27\\-0.33\\0.89\end{pmatrix}$
C axis Euler angle (EBSD)	φ1=33° Φ=20°	φ1=305° Φ=36°	φ1=191° Φ=40°	φ1=75° Φ=43°	φ1=157° Φ=45°
Shape of the ellipse (CPLM)	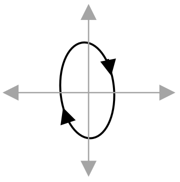	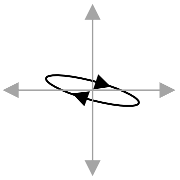	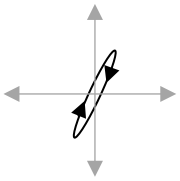	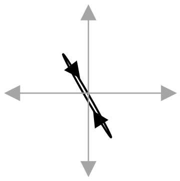	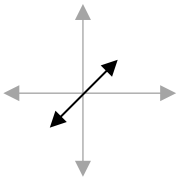
Maximum intensity angle(CPLM)	175°	105°	25°	150°	45°
Stoke parameters	$S_{out}=\begin{pmatrix}1\\0.63\\-0.11\\0.76\end{pmatrix}$	$S_{out}=\begin{pmatrix}1\\-0.82\\-0.475\\0.31\end{pmatrix}$	$S_{out}=\begin{pmatrix}1\\0.63\\0.75\\0.17\end{pmatrix}$	$S_{out}=\begin{pmatrix}1\\0.5\\-0.86\\0.069\end{pmatrix}$	$S_{out}=\begin{pmatrix}1\\0\\1\\0\end{pmatrix}$

3.4 Crystal orientation maps

The final stage is to compare the crystal orientation maps directly between the CPLM method and the EBSD method (Fig. 12). A MATLAB code analyzed images recorded at all analyser positions pixel by pixel. Each pixel position for the dataset therefore contains information on the whole intensity profile. The position of maximum intensity and ΔI were determined and used via the approach presented above to calculate $\varphi 1$ and Φ for every pixel position. To obtain a comparative EBSD map based solely on [001] directions, a 'basal pole figure' colouration was employed in which orientations are plotted according to stereographic projections onto the colour wheel. According to the Euler map from EBSD (Fig. 12A), the red channel corresponds to the value of $\varphi 1$, and the green channel represents the value of Φ. This colour convention was used to create an equivalent map from CPLM data. In this case the value of $\varphi 2$ is irrelevant because it represents the rotation around the HCP c-axis (FCC [001] direction) which cannot be resolved by the CPLM technique.

The CPLM method simplifies data collection and removes the necessity for step size determination, i.e. data is collected at a consistent resolution determined by the wavelength of the monochromatic light source (440*n*m). The orientations of each crystal are clearly distinguished by CPLM method and validated by EBSD, however there are some differences. The highlighted CPLM grains appear as different colours compared to the EBSD map, but this is not due to any errors in the CPLM approach. The CPLM method utilizes the symmetry of the cubic unit cell. However, post-processing EBSD packages such as Tango, Crystal Aztech and TSL report crystallographic data with respect to the Euler twist [45,50-52]. The absence of a standard symmetry for the unit cell causes the above programs to represent the grains with different Euler colours although they may have the very similar orientations. This particular error is described in detail by [49,50] and is highlighted by this CPLM technique. The difference becomes more noticeable when $\varphi 1>300°$, e.g. the highlighted crystals in Fig. 12A all have their $\varphi 1>330°$, according to crystal symmetry they should be treated the same as crystals with $\varphi 1>150°$.

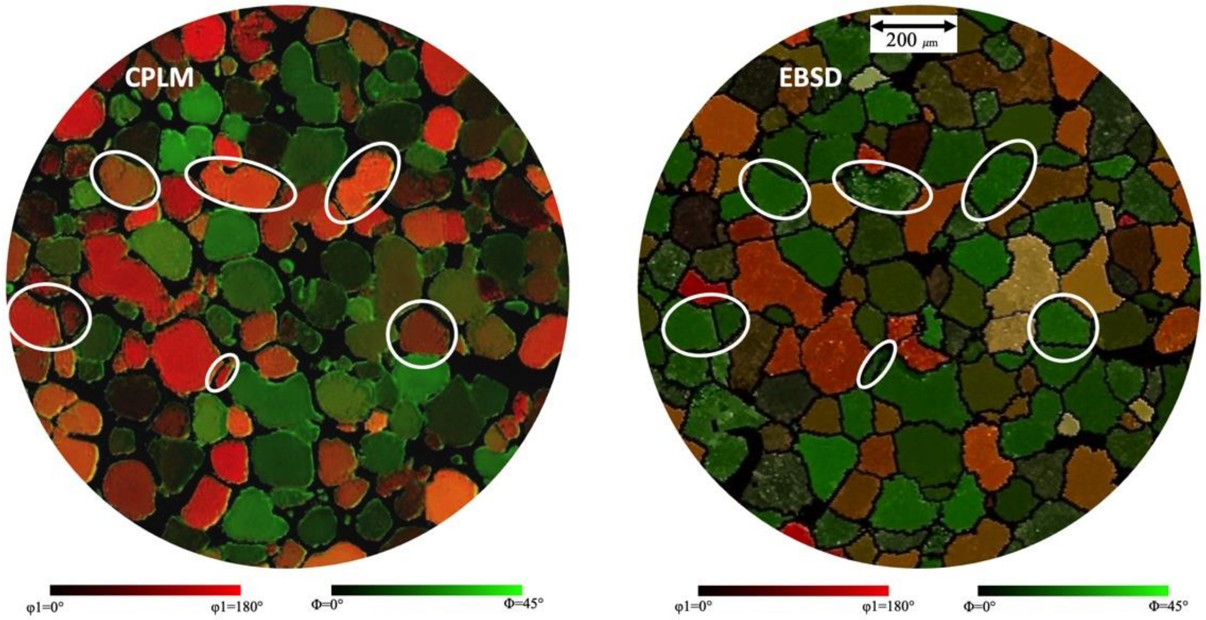

A) B)

Fig. 12. The c-axis crystal orientations maps from the same sample area by using the CPLM method and EBSD. A) represents the crystal orientation map by using the CPLM method and B) illustrates Crystal Orientation Map by using the EBSD method.

3.5 Impact of anodization on the technique

As is presented, anodized aluminium alloys become optically anisotropic under polarized light microscopy due to the light interaction with the oxide film on the grain surface. The light reflection from the anodized surface and the interface between the anodic layer and the Al substrate intertwined with scattering and absorption within the anodic layer generates a specific optical appearance as has been previously described [17,41-43]. The authors wanted to ensure that the anodization process itself did not have an effect on the measured orientations (i.e. that the previously reported oxide/substrate orientation relationships were preserved). For that reason the entire experiment was repeated after re-polishing (to acquire EBSD data) and re-anodising (to acquire CPLM data) the sample surface (whilst preserving the original section of the microstructure).

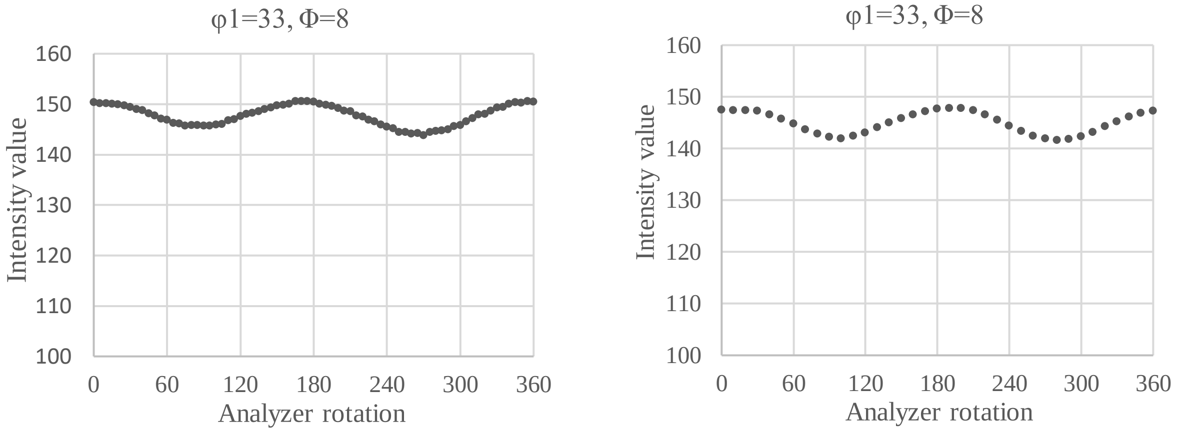

A) B)

Fig. 13. The intensity plots from the same grain. A) First time anodization data collected on every 5° of analyzer rotation. B) Intensity plot of re-anodized grain, data collected on every 10° of analyzer rotation.

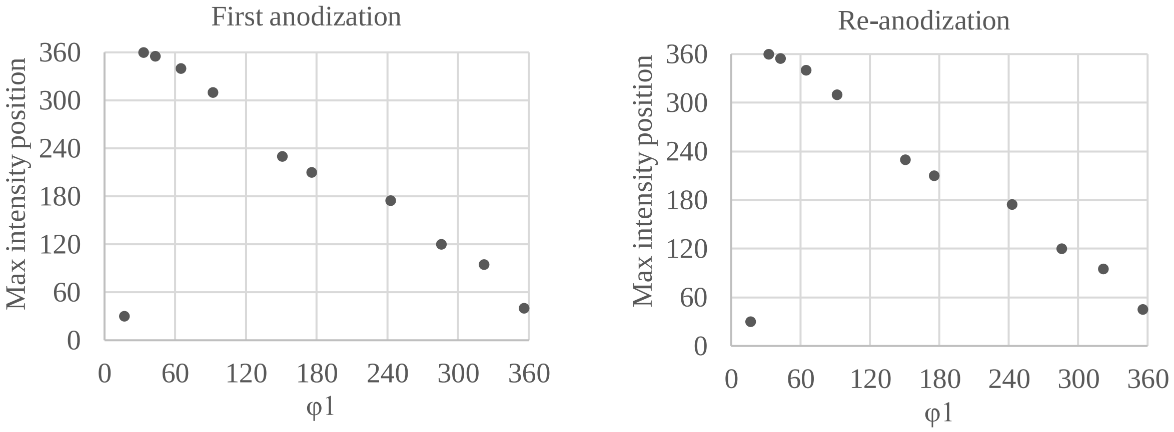

A) B)

Fig. 14. Compared data of maximum intensity position from the first anodization and re-anodized sample.

Figs. 13 and 14 confirmed no significant change in intensity between the first anodization and re-anodization of the same grain. Data was collected for a variety of crystal orientations to confirm the interdependency of the anodized layer and the substrate crystallographic orientation. Each specific grain illustrated identical position of maximum intensity with respect to the analyzer rotations. Also, the data showed each specific grain to maintain identical value for the ΔI unconventionally to the anodized layer [41-44].

4. Conclusions

Four separate analysis techniques (EBSD, bright field optical microscopy, pan-chromatic circular polarized light microscopy and monochromatic circular polarized light microscopy) have been applied to identical areas of microstructure of an FCC Al-Cu alloy in two distinct forms. The CPLM was shown (we believe for the first time) to have the potential to be employed as an accessible, cheap and accurate approach to produce crystal orientation maps of some FCC crystal systems.

- Qualitative comparisons between single images acquired using EBSD and monochromatic CPLM revealed that monochromatic CPLM accurately described areas of common [001] directions for FCC crystal structures (via its orientation relationship with the [0001] direction of the HCP surface oxide generated through anodization). The new method correctly determined the value for Euler 1 (φ1) and Euler 2 (Φ) and the colour system employed plotted green & red colours in close correlation to corresponding EBSD orientation maps. The crystal symmetry of cubic structures helped to optimize the CPLM post processing procedure making this new simplified method more suited for potential quality assurance applications.

- There was some discrepancy in the colour schemes between the two methods which highlights the fundamental limitation of symmetry representation in EBSD Euler maps. However, these differences were not found translate to differences in the underlying orientation data and can therefore be considered as an advantage of the CPLM technique.

- This new method was successfully tested on anodized aluminium, which historically provides challenges for good EBSD orientation data. It was found that the re-anodizing of aluminium had little effect on the subsequent crystal orientation provided the anodizing parameters remained consistent.

- The oxide-substrate orientation relationship on which the current study builds was previously determined for a limited number of orientation combinations due to the complexity of extracting orientation data from surface layers of nanoscale thickness by HRTEM. The current study replicated the prior finding with a comparatively trivial technique, indicating its significant potential to study other such interfaces in the future.

References.

1. Kuroda M. Effects of Texture on Mechanical Properties of Aluminum Alloy Sheets and Texture Optimization Strategy. 2005.
2. Zhang L, Wang Y, Yang X, Li K, Ni S, Du Y, et al. Texture, microstructure and mechanical properties of 6111 aluminum alloy subject to rolling deformation. Mater Res. 2017 Oct 1;20(5):1360–8.
3. Nakashima PNH. The Crystallography of Aluminium and its Alloys. arXiv. 2020. 1–93 p.
4. Britton TB, Jiang J, Guo Y, Vilalta-Clemente A, Wallis D, Hansen LN, et al. Tutorial: Crystal orientations and EBSD - Or which way is up? Mater Charact [Internet]. 2016;117(April):113–26. Available from: http://dx.doi.org/10.1016/j.matchar.2016.04.008
5. Boehm-Courjault E, Gonzales F, Jacot A, Kohler F, Mariaux A, Niederberger C, et al. EBSD: A powerful microstructure analysis technique in the field of solidification. J Microsc. 2009;233(1):160–9.
6. Callahan PG, Echlin M, Pollock TM, Singh S, De Graef M. Three-dimensional texture visualization approaches: Theoretical analysis and examples. J Appl Crystallogr. 2017;50:430–40.
7. Collett E. Field Guide to Polarization. Field Guide to Polarization. 2009.
8. Curtis RK, Tyson DONR. Birefringence : Polarization Microscopy as a Quantitative Technique of Human Hair Analysis. J Soc Cosmet Chem. 1976;27(9):411–31.
9. Ross S, Newton R, Zhou YM, Haffegee J, Ho MW, Bolton JP, et al. Quantitative image analysis of birefringent biological material. J Microsc. 1997;187(1):62–7.
10. Whittaker P, Przyklenk K. Fibrin architecture in clots: A quantitative polarized light microscopy analysis. Blood Cells, Mol Dis [Internet]. 2009;42(1):51–6. Available from: http://dx.doi.org/10.1016/j.bcmd.2008.10.014
11. Shribak M, Oldenbourg R. Techniques for fast and sensitive measurements of two-dimensional birefringence distributions. Appl Opt. 2003;42(16):3009.
12. Safaie H, Mitchell RL, Johnston R, Russell J, Pleydell-Pearce C. An Assessment of Polarized Light Microscopy for the Quantification of Grain Size and Orientation in Titanium Alloys via Microanalytical Correlative Light to Electron Microscopy (CLEM). Microsc Microanal. 2018 Aug;24(S1):400–1.
13. Böhme L, Morales-Rivas L, Diederichs S, Kerscher E. Crystal c-axis mapping of hcp metals by conventional reflected polarized light microscopy: Application to untextured and textured cp-Titanium. Mater Charact [Internet]. 2018;145(July):573–81. Available from: https://doi.org/10.1016/j.matchar.2018.09.024
14. Nafisi S, Roccisano A, Ghomashchi R, Voort G Vander. A comparison between anodizing and EBSD techniques for primary particle size measurement. Metals (Basel). 2019 May 1;9(5).
15. Maitland T, Sitzman S. (EBSD) Technique and Materials Characterization Examples. :41–76.
16. Safaie H, Mitchell RL, Johnston R, Russell J, Pleydell-Pearce C. An Assessment of Polarized Light Microscopy for the Quantification of Grain Size and Orientation in Titanium Alloys via Microanalytical Correlative Light to Electron Microscopy (CLEM). Microsc Microanal. 2018;24(S1):400–1.
17. Newton CJ, Vacher HC. Correlation of Polarized Light Phenomena With the Orientation of Some Metal Crystals. Vol. 53, Journal of Research of the National Bureau of Standards. 1954.

18. Donatus U, Thompson GE, Elabar D, Hashimoto T, Morsch S. Features in aluminium alloy grains and their effects on anodizing and corrosion. Surf Coatings Technol. 2015 Sep 15;277:91–8.
19. Nolze G. Image distortions in SEM and their influences on EBSD measurements. Ultramicroscopy. 2007;107(2–3):172–83.
20. Seshagiri PC, Nair BS, Reddy GM, Rao KS, Bhattacharya SS, Rao KP. Improvement of mechanical properties of aluminium-copper alloy (AA2219) GTA welds by Sc addition. Sci Technol Weld Join. 2008 Mar;13(2):146–58.
21. Koll L, Tsipouridis P, Werner EA. Preparation of metallic samples for electron backscatter diffraction and its influence on measured misorientation. J Microsc. 2011;243(2):206–19.
22. Wielage B, Alisch G, Lampke T, Nickel D. Anodizing - A key for surface treatment of aluminium. Key Eng Mater. 2008;384:263–81.
23. Ambroziak A, Solarczyk MT. Application and mechanical properties of aluminium alloys. Shell Struct Theory Appl Vol 4 - Proc 11th Int Conf Shell Struct Theory Appl SSTA 2017. 2018;(May 2020):525–8.
24. Zhou\ X[, Thompson E[, Skeldon A\ \ G[c[Wood P[, Shimizu K[, Habazaki H[. Anodic oxidation of an AlÐ1 wt) Cu alloy] e}ect of grain orientation.
25. Danz R, Gretscher P. C-DIC: A new microscopy method for rational study of phase structures in incident light arrangement. Thin Solid Films. 2004;462–463(SPEC. ISS.):257–62.
26. Higgins MD. Imaging birefringent minerals without extinction using circularly polarized light. Can Mineral. 2010;48(1):231–5.
27. Theofanous NG. Error analysis of circular polarizer–analyzer systems for phase retardation measurements. J Opt Soc Am A. 2008;4(12):2191.
28. Modern Optics Simplified - Robert D. Guenther - Google Books.
29. Hu Y, Yi Z, Yang H, Xiao J. A simple method to measure the thickness and order number of a wave plate. Eur J Phys. 2013 Sep;34(5):1167–73.
30. Schaefer B, Collett E, Smyth R, Barrett D, Fraher B. Measuring the Stokes polarization parameters. Am J Phys. 2007 Feb;75(2):163–8.
31. Scott S, Ko J. Polarization Changes by flat, ideal mirrors. 2008;1–27.
32. Agarwal N. Basics of Polarization. 2013;1–28.
33. Abramowitz M. Microscopy: Basics and Beyond. Mol Expressions Microsc Prim [Internet]. 2003;1:1–50. Available from: http://micro.magnet.fsu.edu/primer/index.html
34. Cox AJ. Quantitative analysis of elliptically polarized light. Am J Phys. 1978;46(3):302–3.
35. Ferro-Famil L, Pottier E. SAR Imaging using Coherent Modes of Diversity: SAR Polarimetry, Interferometry and Tomography. Microw Remote Sens L Surfaces Tech Methods. 2016;67–147.
36. Magnusson R. Mueller matrix ellipsometry studies of nanostructured materials. 57 p.
37. Li P, Lv D, He H, Ma H. Separating azimuthal orientation dependence in polarization measurements of anisotropic media. Opt Express. 2018 Feb 19;26(4):3791.
38. Milione G, D'Addario AJ, Jones JA, Galvez EJ, Rojec BL. The Poincaré-sphere approach to polarization: Formalism and new labs with Poincaré beams. Am J Phys. 2016;84(11):822–35.
39. Pizurica A. Pattern Encoding on the Poincare Sphere. 2014;1–26. Available from: http://arxiv.org/abs/1410.0243
40. Suzuki M, Yamane K, Oka K, Toda Y, Morita R. Full Quantitative Analysis of Arbitrary Cylindrically Polarized Pulses by Using Extended Stokes Parameters. Sci

Rep [Internet]. 2015;5(September):1–9. Available from: http://dx.doi.org/10.1038/srep17797

41. Sacco L, Florea I, Châtelet M, Cojocaru CS. Investigation of porous anodic alumina templates formed by anodization of single-crystal aluminum substrates. Thin Solid Films. 2018 Aug 30;660:213–20.
42. Li F, Zhang L, Metzger RM. On the Growth of Highly Ordered Pores in Anodized Aluminum Oxide. 1998.
43. thompson1978.
44. Jensen F, Gudla VC, Kongstad I, Ambat R. High frequency pulse anodising of aluminium: Anodising kinetics and optical appearance. Surf Coatings Technol. 2019;360:222–31.
45. Schwarzer RA. Backscatter and transmission Kikuchi diffraction for materials science. Available from: http://www.ebsd.info/pdf/overview.pdf
46. By Seishi KIKUCHI. Institute of Physical and Chemical Research, Tokyo. (Rec. June 9, 1928. Comm. by T. TERADA, M. I .A., June 12, 1928.). 1928;117(6).
47. Richartz M, Hsü H-Y. Analysis of Elliptical Polarization. J Opt Soc Am. 1949;39(2):136.
48. Chen W, Li H, Zhang S, Long X. Measurement of phase retardation of waveplate online based on laser feedback. Rev Sci Instrum. 2012;83(1):2012–5.
49. Clegg W, Blake AJ, Cole JM, Evans JSO, Main P, Parsons S, et al. Crystal Structure Analysis: Principles and Practice. Cryst Struct Anal Princ Pract. 2009;9780199219:1–408.
50. Nolze G. Euler angles and crystal symmetry. Cryst Res Technol. 2015;50(2):188–201.
51. Randle V. Application of EBSD to the analysis of interface planes: Evolution over the last two decades. J Microsc. 2008;230(3):406–13.
52. Mingard KP, Roebuck B, Bennett EG, Thomas M, Wynne BP, Palmiere EJ. Grain size measurement by EBSD in complex hot deformed metal alloy microstructures. J Microsc. 2007;227(3):298–308.